PHOTONICS Research

Large-area ultracompact pixelated aluminum-wire-grid-based metamaterials for Vis-NIR full-Stokes polarization imaging

Yuanyi Fan,[1,2] Jinkui Chu,[1,2,3] Ran Zhang,[1,2,4] Chuanlong Guan,[1,2] and Jianying Liu[1,2]

[1]State Key Laboratory of High-performance Precision Manufacturing, Dalian University of Technology, Dalian 116024, China
[2]Key Laboratory for Micro/Nano Technology and System of Liaoning Province, Dalian University of Technology, Dalian 116024, China
[3]e-mail: chujk@dlut.edu.cn
[4]e-mail: zhangr@dlut.edu.cn

The study of pixelated metamaterials that integrate both the functions of linear and circular polarization filters is rapidly growing due to the need for full-Stokes polarization imaging. However, there is a lack of large-area, ultra-compact pixelated full-Stokes metamaterials with excellent performance, especially circular polarization filters with a high extinction ratio, a broad operating bandwidth, and a low-cost, high-quality, efficient manufacturing process, which limits the practical applications of pixelated full-Stokes metamaterials. In this study, we propose a universal design and fabrication scheme for large-area, ultracompact pixelated aluminum wire-grid-based meta-materials used in Vis-NIR full-Stokes polarization imaging. The aluminum wire-grid was designed as a linear polarization filter with an average linear polarization extinction ratio of 36,000 and a circular polarization filter with an average circular polarization extinction ratio of 110 in Vis-NIR. A large-area, ultracompact 320×320 pixelated aluminum wire-grid-based full-Stokes metamaterial was fabricated using nanoimprint lithography and nano transfer printing with the advantages of low cost and high efficiency. This metamaterial was used to achieve full-Stokes polarization imaging with errors within 8.77%, 12.58%, 14.04%, and 25.96% for Stokes parameters S_0, S_1, S_2, and S_3, respectively. The inversion errors of the compensated Stokes parameters can be reduced to 0.21%, 0.21%, 0.42%, and 1.96%, respectively.   © 2023 Chinese Laser Press

https://doi.org/10.1364/PRJ.494728

1. INTRODUCTION

Polarization, similar to phase, wavelength, and intensity, is an important parameter of light and essential for applications such as communication [1,2] and quantum encryption [3,4]. Polarization imaging in the Vis-NIR spectral region is especially attractive due to its broad applications in polarization navigation [5,6], biomedical diagnosis [7,8], target detection [9], and face recognition [10,11] with the advantage of revealing the intrinsic properties of matter. Polarization imaging systems are mainly divided into division-of-time, division-of-aperture, division-of-amplitude, and division-of-focal-plane types. In particular, the division-of-focal-plane type has the advantage of good real-time and easy integration, and has gained an in-creasing amount of attention. It is well known that the arbitrary state of polarization (SoP) can be represented by the Stokes parameters (S_0, S_1, S_2, S_3), which are related to the light intensity of the linearly and circularly polarized components of incident light. Currently, the division-of-focal-plane type pixe-lated micro arrays consist of linear polarization filters oriented

in different directions, such as iodine-doped polyvinyl alcohol layer [12], liquid crystals [13], and metal wire-grids [14,15], which have excellent polarization optical performance but can only detect linearly polarized components, not circularly polarized components, so only part of the Stokes parameters (S_0, S_1, S_2) can be detected.

To achieve full-Stokes parameters detection, the main ob-stacle is pixelated micro arrays integrating both the functions of linear polarization filters and circular polarization filters. Methods based on organic materials, such as liquid crystal pol-ymer [16] and chiral organic molecules [17], enable detection of circularly polarized components, which are usually incom-patible with scalable manufacturing technology, structurally and chemically unstable, or highly absorptive in mid-IR spec-tral regions. Metamaterials or metasurfaces with subwavelength spacing and dimensions have unusual electromagnetic proper-ties, providing a powerful toolbox for implementing many dif-ferent electromagnetic wave operations, such as perfect absorption, flat lensing, holograms, and polarization transfor-mation. Chiral optical metamaterials from two-dimensional

(2D) to three-dimensional (3D) exhibit a mixture of magnetic and electrical responses excited by a light field, and can be designed to achieve strong CD [the differential absorption or transmission of left-handed and right-handed circularly polarized light (LCP and RCP)] and used as high-performance circular polarizer filters. However, 2D planar chiral or achiral structures [18–21] are limited to narrow frequency responses originating from the internal resonances of individual building blocks, which is a major drawback for many potential applications. 3D helix chiral structures [22–28] including the single-helix, double-helix, N-helix, tapered helix, and hybrid helix, combine internal and Bragg resonances leading to a broadband response, while realizing these smaller nanostructures in the visible region imposes higher requirements on the resolution of direct laser writing. To cope with this problem, researchers have made some new efforts. In terms of structural design, substituting helix chiral structures with stacked planar metasurfaces [29–31] may effectively operate as 3D helical structures with broadband CD optical responses and can be realized with conventional lithographic techniques, but periodic arrays with precise alignment and subwavelength features are still challenging at visible wavelengths. For the fabrication process, cost-effective and simple bottom-up methods [32–34] such as glancing angle deposition and grazing incidence were introduced to fabricate long-range ordered chiral structures over large areas, yet the CD optical effects in these structures are relatively weak. More recently, a combination of dielectric or plasma-based quarter-wave plates and metallic wire-grid linear polarization filters [35,36], realized by electron beam lithography, reactive-ion etching or lift-off, etc., has been used for full-Stokes polarization detection. The quarter-wave plate has a narrow operating bandwidth, and the inconsistent structural form or material with wire-grid-based linear polarization filters leads to an inconsistent fabrication process or high fabrication cost. In summary, the challenges to realize full-Stokes polarization imaging mainly include: (1) the structural form of broadband circular polarization filters with excellent performance is complicated, and it is difficult to realize large-area, low-cost, and high-precision fabrication; (2) circular polarization filters and linear polarization filters are not consistent in terms of material and structural form, and the fabrication processes are not compatible; (3) current full-Stokes polarization detection units are fabricated by electron beam lithography combined with reactive-ion etching or lift-off, which is characterized by high cost and time consumption, making it difficult to manufacture large-area ultracompact pixelated division-of-focal-plane devices for full-Stokes polarization imaging.

In this paper, we propose and experimentally demonstrate a large-area ultracompact pixelated aluminium wire-grid-based metamaterial for Vis-NIR full-Stokes polarization imaging. The pixelated metamaterial integrates the functions of both linear and circular polarization filters. In the design of linear polarization filters, based on the broadband polarization-selective transmittance of sub-wavelength wire-grid-based metamaterials [37], the designed wire-grid linear polarization filter achieved an average linear polarization extinction ratio of 36,000 in the 400–1200 nm bandwidth. In the design of circular polarization filters, based on the physical phenomenon

that self-complementary metamaterials [38] produce a 90° phase difference independent of wavelength between TM and TE polarized light, a broadband aluminium wire-grid-based circular–linear polarization converter [39] was designed, and it was further cascaded with the above mentioned linear polarization filter to realize a broadband circular polarization filter (average circular polarization extinction ratio of 110 in the 400–1200 nm bandwidth). Furthermore, both linear and circular polarization filters are structured by an aluminium wire-grid, which can be fabricated by nanoimprint lithography, and metal transfer to achieve large-area on-chip integration with the advantages of low cost, high quality, and high efficiency. The design features an ultracompact layout and excellent polarization optics performance and capability of easy integration onto various types of Vis-NIR imaging detectors.

2. DEVICE DESIGN

The device proposed here for full-Stokes polarization imaging is based on large-area ultracompact pixelated aluminium wire-grid-based metamaterials, as shown in Fig. 1(a). It consists of 320×320 microcells, with each neighboring four microcells forming a supercell containing three differently oriented linear polarization filters (F_1, F_2, and F_3) and a circular polarization filter (F_4). $F_1 – F_3$ microcells are linear polarization filters to filter linear polarization light with the electric field vector oriented at different angles with respect to the x axis, i.e., LP = 0°, 45°, and 90°. The F_4 microcell is a left circular polarization filter to transmit circular polarization light with the electric field vector trajectory oriented anti-clockwise. The handedness of circular polarization light was defined from the point of view of the receiver. The right-handedness corresponds to a clockwise rotation, and the left-handedness corresponds to an anti-clockwise rotation. Figure 1(b) shows one of the linear polarization filters (F_1), which is based on a double-layer aluminium wire-grid with geometric parameters period P_1, wire width W_1, height H_1, and spacing D_1. The linear polarization light with an electric vector perpendicular to the wire-grid is defined as TM light, and the polarized light with an electric vector parallel to the wire-grid direction is defined as TE light. As we can see in Fig. 1(b), TM polarized light passes through the wire-grid region, while TE polarized light is confined to the wire-grid region. Therefore, the linear polarization filters can filter out TE light and transmit TM light. Figure 1(c) shows the circular polarization filter (F_4), which consists of a surface layer circular–linear polarization converter and a bottom layer linear polarization filter with a 45° relative angle. The period, wire width, wire height, and spacing from the underlying linear polarization filter of the surface layer circular–linear polarization converter are denoted as P_2, W_2, H_2, and D_2, respectively.

Linear polarization filters based on metal wire-grids have been extensively explored. In this paper, the metal wire-grid has a period of 200 nm and a wire width of 100 nm, where the period is less than half a wavelength to avoid optical diffraction. The optical properties of single- and double-layer linear polarization filters with varying heights H_1 of aluminium wire-grids in the Vis-NIR were analyzed by the finite difference time domain (FDTD) method, as shown in Fig. 2. The spacing D_1 of the bilayer wire-grid is set to a fixed value of 200 nm.
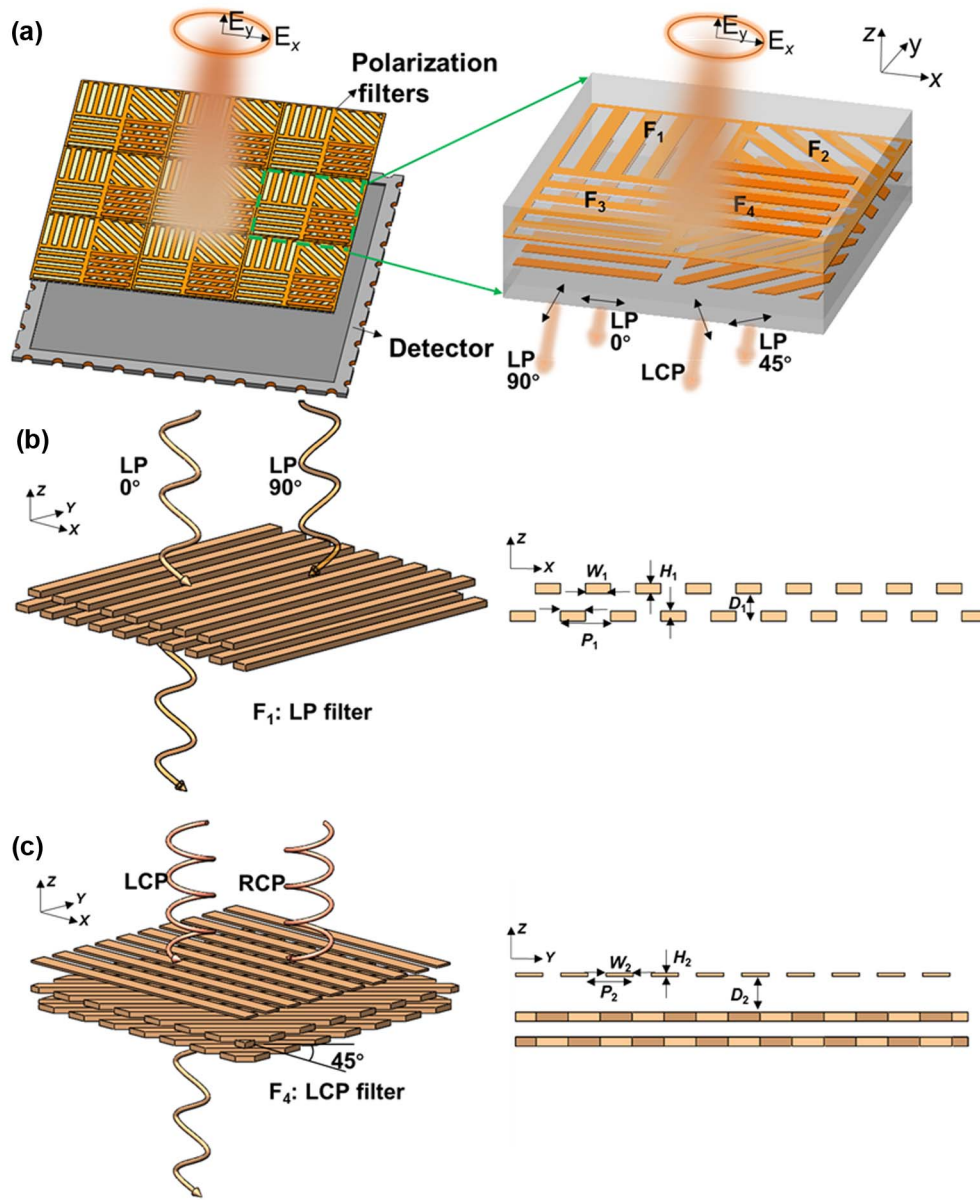
Fig. 1. Large-area ultracompact pixelated aluminium wire-grid-based metamaterials for full-Stokes polarization imaging. (a) Schematic of the device design for Stokes parameters measurement. $F_1 – F_3$ microcells are linear polarization filters to filter linearly polarized light with the electric field vector oriented at different angles with respect to the x axis, i.e., 0°, 45°, and 90°. F_4 microcell is left circular polarization filter to transmit left circular polarization light. (b) Schematic of the linear polarization filters consisting of the double-layer wire-grid. The period, wire width, height, and spacing are P_1, W_1, H_1, and D_1, respectively. (c) Schematic of the left circular polarization filter consisting of a top circular–linear polarization converter and an underneath linear polarization filter. The period, wire width, height of the circular–linear polarization converter, and spacing between the circular–linear polarization converter and the linear polarization filter are P_2, W_3, H_2, and D_2, respectively.

T_{TM} and T_{TE} denote the transmission of TM and TE light by the linear polarization filter, respectively. The linear polarization extinction ratio is defined as T_{TM}/T_{TE}. Figures 2(a) and 2(d) show that the transmittance of TM light is of the same order of magnitude for the double-layer and single-layer nano wire-grid-based linear polarization filters. Figures 2(c) and 2(f) show that double-layer nano wire-grid-based linear polarization filters usually have a higher extinction ratio. In addition, for the double-layer structure, the extinction ratio increases with increasing thickness, but the transmittance of TM light tends to decrease when the height of the wire-grid is greater than 80 nm. In order to obtain a large TM light transmittance and a wide operating bandwidth while ensuring a large extinction ratio, a double-layer nano wire-grid-based linear polarization filter with geometrical parameters of 200 nm period, 100 nm wire width, and 80 nm wire height was finally used, for which the average linear polarization extinction ratio of the linear polarization filter reached 36,000 in the visible near-infrared wavelength range.

Circular polarization filters consist of circular linear polarization converters and linear polarization filters. The circular linear polarization converter based on a single-layer metal nano
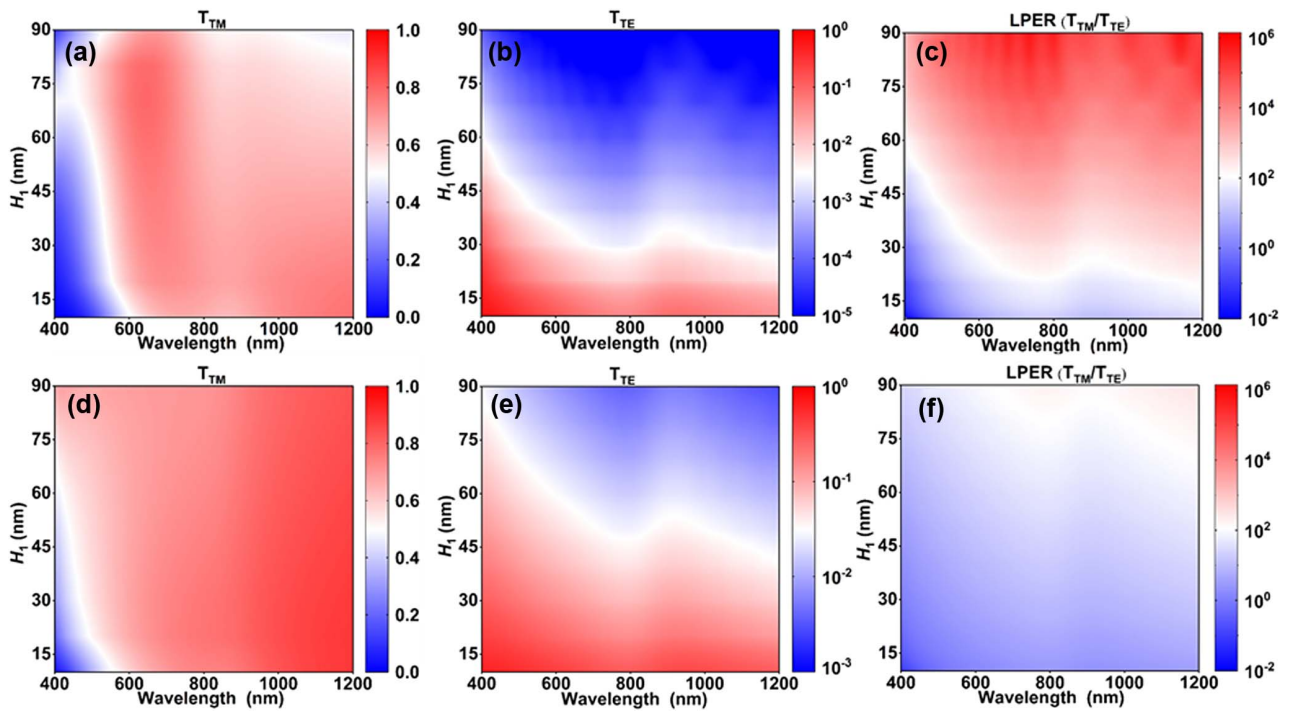
Fig. 2. Optical parameters of the double-layer nano wire-grid linear polarization filter: (a) TM light transmission, (b) TE light transmission, and (c) linear polarization extinction ratio. Optical parameters of the single-layer nano wire-grid polarization filter: (d) TM light transmission, (e) TE light transmission, and (f) linear polarization extinction ratio. The geometric parameters of the wire-grid are 200 nm period and 100 nm wire width. The spacing between the bilayer wire grids $D_1 = 200$ nm. Aluminium wire-grid height H_1 varies from 10 to 90 nm.

wire-grid can produce a phase difference of 90° between TM and TE light in a wide bandwidth. Its geometric parameters are 180 nm period, 120 nm wire width, and 12 nm wire height [39]. The circular polarization filter has been deduced to have circular dichroism over a wide bandwidth and reaches a maximum at an angle of 45° between the circular linear polarization converter and the linear polarization filter [40]. In the design of the circular polarization filter in this paper, the circular linear polarization converter is integrated into the linear polarization filter, and the light field reflection and interference between the two will occur. Therefore, the influence of the spacing between the circular linear polarization converter and the linear polarization filter on the circular dichroism and circular polarization extinction ratio is further analyzed by FDTD in conjunction with the thin-film interference model (for the analytical method, refer to our earlier paper [40]). The optical properties of circular polarization filters in the visible near-infrared band with varying D_2 are given in Fig. 3. The transmittance of the circular polarization filter for left- and right-handed circular polarization light is shown in Figs. 3(a) and 3(b), respectively. It can be found that the transmittance of LCP is greater than that of RCP in a wide bandwidth, which shows that it has broadband circular dichroism. As shown in Figs. 3(c) and 3(d), both circular dichroism and circular polarization extinction ratio peaks are redshifted as the spacing D_2 increases, which provides design freedom for us to design the dominant working wavelength of a circular polarization filter. Especially, the circular polarization extinction ratio exceeds 1000 near 780 nm wavelength when D_2 is 200 nm, and the average circular

polarization extinction ratio reaches 110 in the whole Vis-NIR band. The performance of this circular polarizer has certain advantages. In addition, both the designed linear polarization filter and circular polarization filter are based on a nano wire-grid structure, which can be fabricated by interference lithography, nanoimprint lithography, or nano transfer printing with the advantages of large area and low cost.

3. DEVICE FABRICATION AND CHARACTERIZATION

In our design, both linear polarization and circular polarization filters are based on an aluminium wire-grid structure and have a low depth-to-width ratio, which can significantly simplify and reduce manufacturing difficulties. The challenges of sample fabrication are large area, cross-scale, and high resolution. In the fabrication, large-area, cross-scale, and high-resolution ultracompact pixelated aluminium wire-grid-based metamaterials were fabricated by nanoimprint lithography, vertical thermal evaporation, and nano transfer printing with the advantages of low cost and high efficiency. The intermediate polymer sheet (IPS) flexible template contains 320 × 320 microcells, and only four adjacent microcells containing wire-grids with different orientations are shown here, as illustrated in Fig. 4(a1). Figures 5(a1) and 5(a2) give the SEM surface images of the IPS flexible template for a micro array with a period size of 20.8 μm × 20.8 μm in the x and y directions and a structured region size of 20 μm × 20 μm. The four adjacent cells are line grids in 0°, 45°, 90°, and −45° directions. The fabrication parameters of the IPS flexible template are given in Ref. [14].
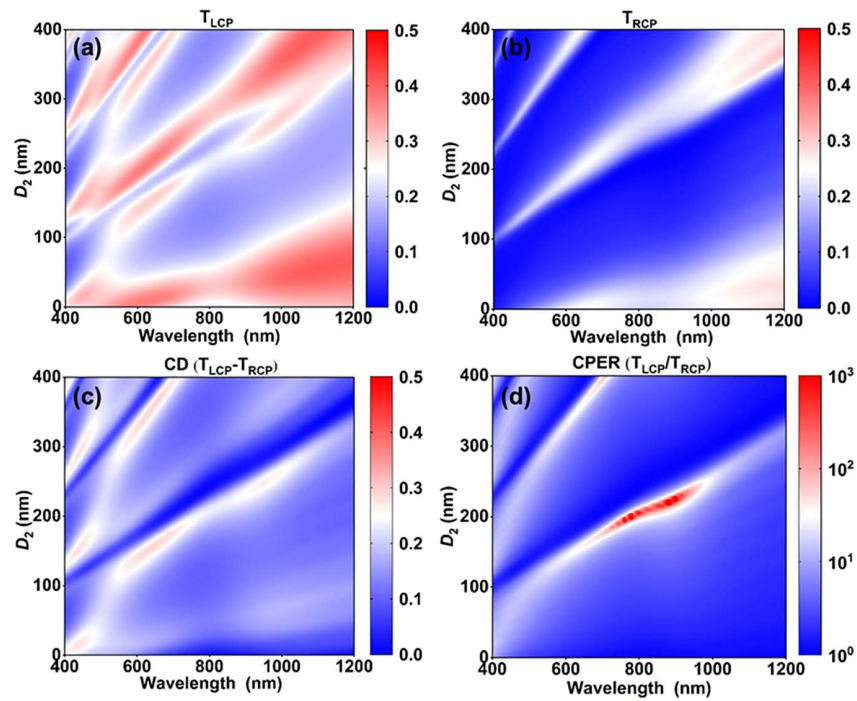
Fig. 3. Simulated optical properties of circular polarization filter with diffrrent D_2. (a), (b) Transmittance spectra of LCP and RCP by full-wave (400–1200 nm) simulation. (c), (d) Circular dichroism (CD = $T_{LCP} - T_{RCP}$) and circular polarization extinction ratio (CPER = T_{LCP}/T_{RCP}) obtained by the transmittance of LCP and RCP.

In this paper, the IPS flexible template was used as a master template. First, the IPS wire-grid structure was transferred onto the quartz substrate by UV-curable nanoimprint lithography with a precoated UV-curable photoresist [Fig. 4(a2)]. The

SEM surface view of the UV-curable nanoimprint photoresist is given in Fig. 5(b). Then the linear polarization filter micro arrays based on double-layer metal-aluminum nano wire-grids were obtained by a vertical thermal vapor deposition process on
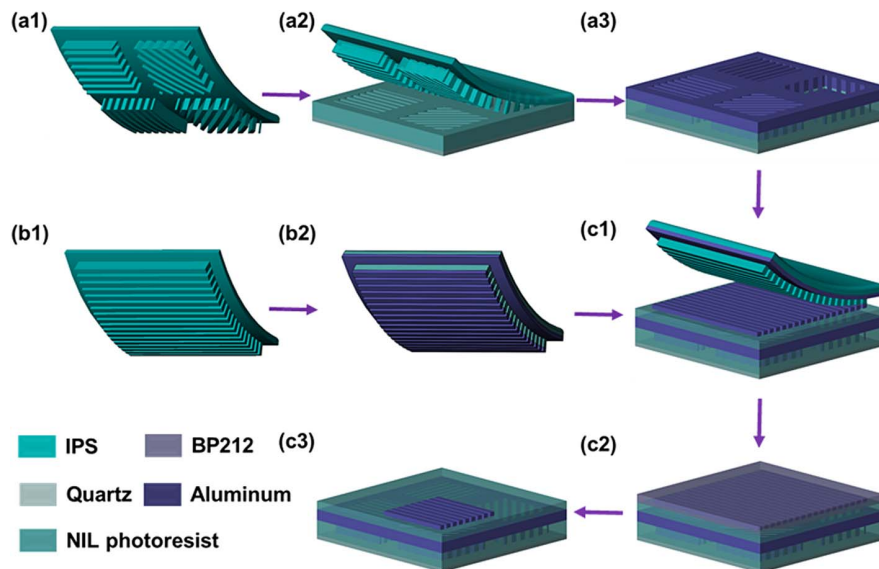

Fig. 4. Device fabrication. (a1) Preparation of IPS flexible template with 0°, 45°, 90°, and –45° orientation wire-grids. (a2) Formation of dielectric wire-grid on the quartz substrate precoated with UV-curable photoresist by UV-curable NIL. (a3) Aluminium wire-grid-based linear polarization filter micro arrays obtained by vertical thermal evaporation process. (b1) Preparation of large-area IPS flexible template with single-directional wire-grid. (b2) Aluminium wire-grid structure obtained by vertical thermal evaporation process. (c1) IPS surface metal nano wire-grid integrated onto the surface of the double-layer metal-aluminum nano wire-grid linear polarization filter micro array precoated with UV-curable photoresist by a nano transfer printing process. (c2) Spin-coating of BP212 on linear polarization filter micro array. (c3) Formation of pixelated metamaterials integrating both the linear polarization filters and circular polarization filters by photolithography, development, etching, and residual adhesive removal process.
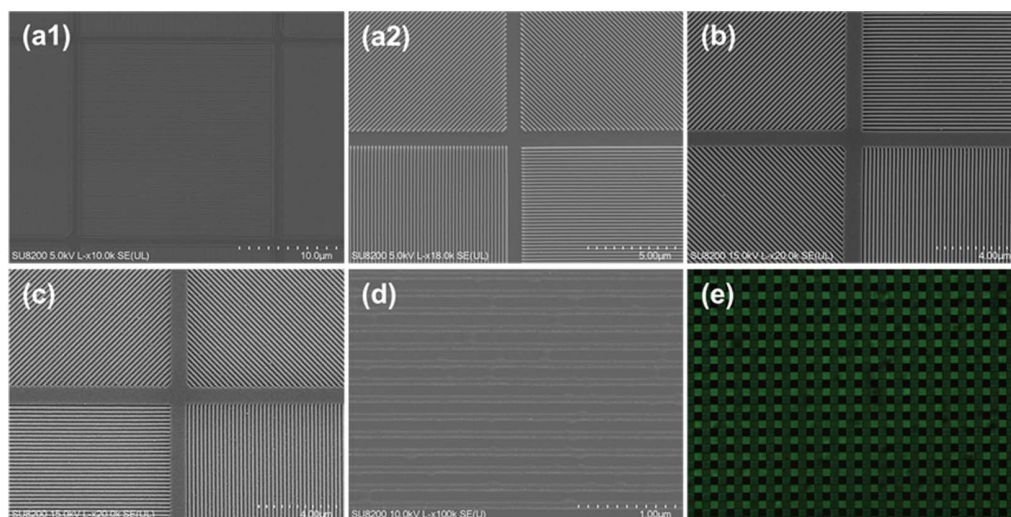
Fig. 5. (a1), (a2) SEM surface views of IPS flexible template with 0°, 45°, 90°, and –45° orientation wire-grids. (b) SEM surface view of the UV-curable nanoimprint photoresist patterned with wire-grid structure. (c) SEM surface view of the aluminium nano wire-grids. (d) SEM surface view of the circular linear polarization converter. (e) Polarization micrograph of the prepared sample.

the quartz target substrate [Fig. 4(a3)]. Figure 5(c) gives the SEM surface view of the metallic aluminum nano wire-grid with a period of 200 nm, a wire width of 100 nm, and a wire height of 80 nm. Figure 4(b1) shows a large area of the IPS flexible template with a single-directional wire-grid structure. First, a double-layer metal-aluminum nano wire-grid is obtained on the surface of the IPS flexible template by a vertical thermal vapor deposition process [Fig. 4(b2)]. Then the IPS surface metal nano wire-grid is transferred to the surface of the double-layer metal-aluminum nanogrid linear polarization filter micro array by a nano transfer printing process with a precoated UV-curable photoresist [Fig. 4(c1)]. Subsequently, BP212 UV photoresist [Fig. 4(c2)] was spin-coated on its surface. Finally, the designed sample was obtained by photolithography, development, etching, and a residual adhesive removal process [Fig. 4(c3)]. The SEM surface view of the sample is given in Fig. 5(d), where the structural region is the surface circular linear polarization converter. Figure 5(e) shows the polarization micrograph of the prepared sample. The detailed process parameters of sample fabrication are given in Appendix A.

The optical properties of the fabricated device are characterized by a measurement system that consists of a light source system and an imaging system, as shown in Fig. 6(a). The light source system is used to produce standard polarized light, such as linearly polarized light, circularly polarized light, and elliptically polarized light, and the system consists mainly of an integrating sphere light source, two filters, a commercial linear polarization filter, a quarter-wave plate, and two precision turntables. The imaging system consists mainly of a camera lens, relay lens, and a monochrome camera. A micro array device was placed in the object plane of the relay lens, which is also the image plane of the lens. The corresponding parameters of the main components are given in Table 1. In the measurement process, linearly polarized light of 0°–180° generated by the light source system was first detected by the imaging system. The azimuthal interval of the linearly polarized light was 5°. Taking into account the simulation results of the polarization device in the broadband of Vis-NIR, we use two narrowband filters with operating wavelengths of 810 and 740 nm to verify the polarization optical performance of the division-of-focal-plane polarization device at different wavelengths. Figure 6(b) gives an example diagram of the imaging system imaging polarized light. Figure 7(a) shows the grayscale value response curves of the three selected $F_1 - F_3$ linear polarization filter
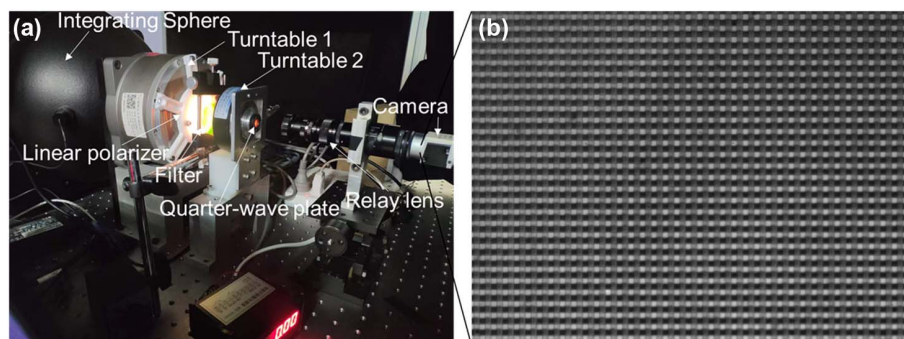

Fig. 6. (a) Experimental diagram of the fabricated device measurement system. (b) Example diagram of the imaging system imaging polarized light.

Table 1. Parameters of Main Components

Component	Parameter	Index
Integrating sphere	Spectral range	350–1100 nm
	Uniformity	±1.0%
	Supplier	Felles Photonic
Filter	Operating wavelength	810 and 740 nm
	Semi-high bandwidth	25 nm
	Supplier	GiAi
Linear polarizer	Extinction ratio	>1000:1
	Transmission	>60%
	Wavelength range	700–1700 nm
	Supplier	Edmund
Quarter-wave plate	Operating wavelength	350–850 nm
	Supplier	Thorlabs
Precision turntable 1	Angle resolution	0.01°
	Rotation angle range	360°
	Supplier	Parker Hannifin
Precision turntable 2	Angle resolution	0.05°
	Rotation angle range	360°
	Supplier	Avantes
Camera lens	Focal length	8–50 mm
	Format	1/2.3″
Relay lens	Magnification	1:1
	Supplier	Edmund
Camera	Sensor	Vendor Sony
	Resolution ($H \times V$)	4024 px × 3036 px
	Pixel size ($H \times V$)	1.85 µm × 1 µm

regions with different azimuthal angles of linear polarization light (810 nm). Based on the grayscale value response curves, the extinction ratios (ratio of maximum to minimum value [14,15]) of $F_1 - F_3$ linear polarization filters were calculated as 14.5, 15.4, and 10.8, respectively. Next, the left- and

right-handed circularly polarized light produced by the light source system was detected by the imaging system. Figure 7(b) shows the grayscale value response of the selected multiple F_4 circular polarization filter with different chiral circularly polarized light (810 nm). According to the grayscale value, the circular polarization extinction ratio was calculated to be about 8.6. Figures 7(c) and 7(d) give the experimental results for a filter operating at 740 nm. Based on the grayscale value response curves, the extinction ratios of $F_1 - F_3$ linear polarization filters were calculated as 8.5, 9.0, and 7.1, respectively. The circular polarization extinction ratio was calculated to be about 5.5. The discrepancy between measurement results and simulation results is mainly related to non-vertical incidence of the light source, camera noise, and depolarization effect of the lens.

The response curves show that the transmittance and extinction ratio optical performance parameters of each microcell are not consistent. This is due to the different forces on the wire-grid cells in different directions during the nanoimprint lithography demolding process, resulting in different optical properties. Therefore, the imaging system needs to be calibrated to achieve full-Stokes polarization imaging. The detailed calibration procedure is given in Appendix B. In addition, since some pixel points in an image only record the information of their corresponding polarization filters, the corresponding information in other directions cannot be acquired at the same time. In this paper, the spatial resolution loss caused by this problem was solved by convolution interpolation [41]. After obtaining the calibrated system matrix, experimental validation of the calibration effect is conducted. The validation experiment parameters are as follows: the azimuth of precision turntable 1 is 0°, the rotation angle range of precision turntable 2 is 0°–180°,
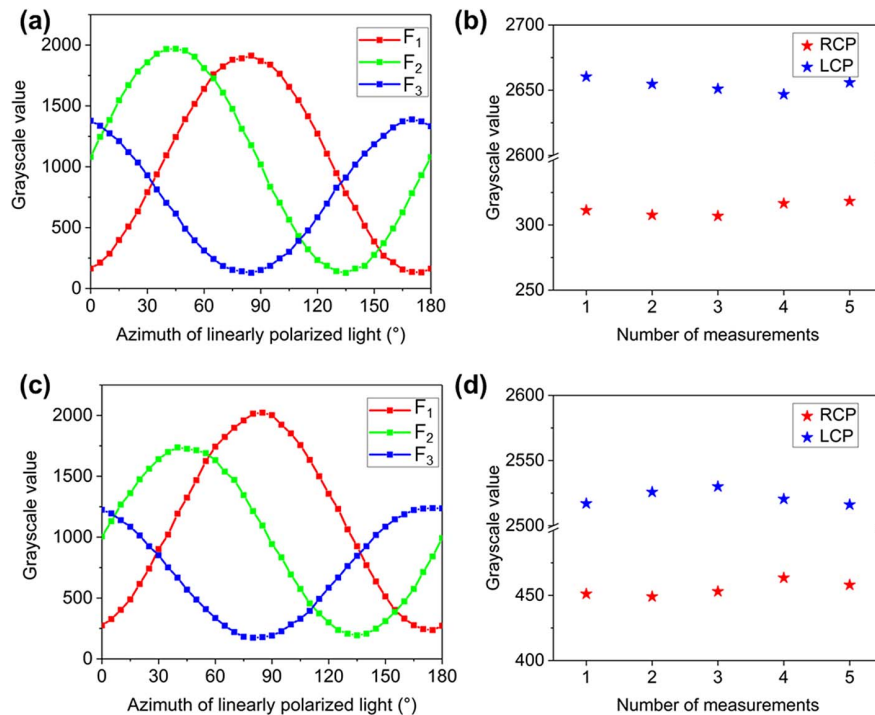

Fig. 7. (a), (c) Grayscale value response curves of the three F_1–F_3 linear polarization filter regions with different azimuthal angles of linear polarization light. (b), (d) Grayscale value response of the F_4 circular polarization filter with different chiral circularly polarized light. (a), (b) The filter operates at a wavelength of 810 nm. (c), (d) The filter operates at a wavelength of 740 nm.

and the step angle is 5°. The incident light's Stokes parameters $S_0 - S_3$ are inverted separately using the system matrix before and after calibration. As shown in Fig. 8, the inverted Stokes parameters $S_0 - S_3$ and their corresponding inversion deviations are given separately. It can be seen that the Stokes parameters inverted by the system matrix before calibration have large
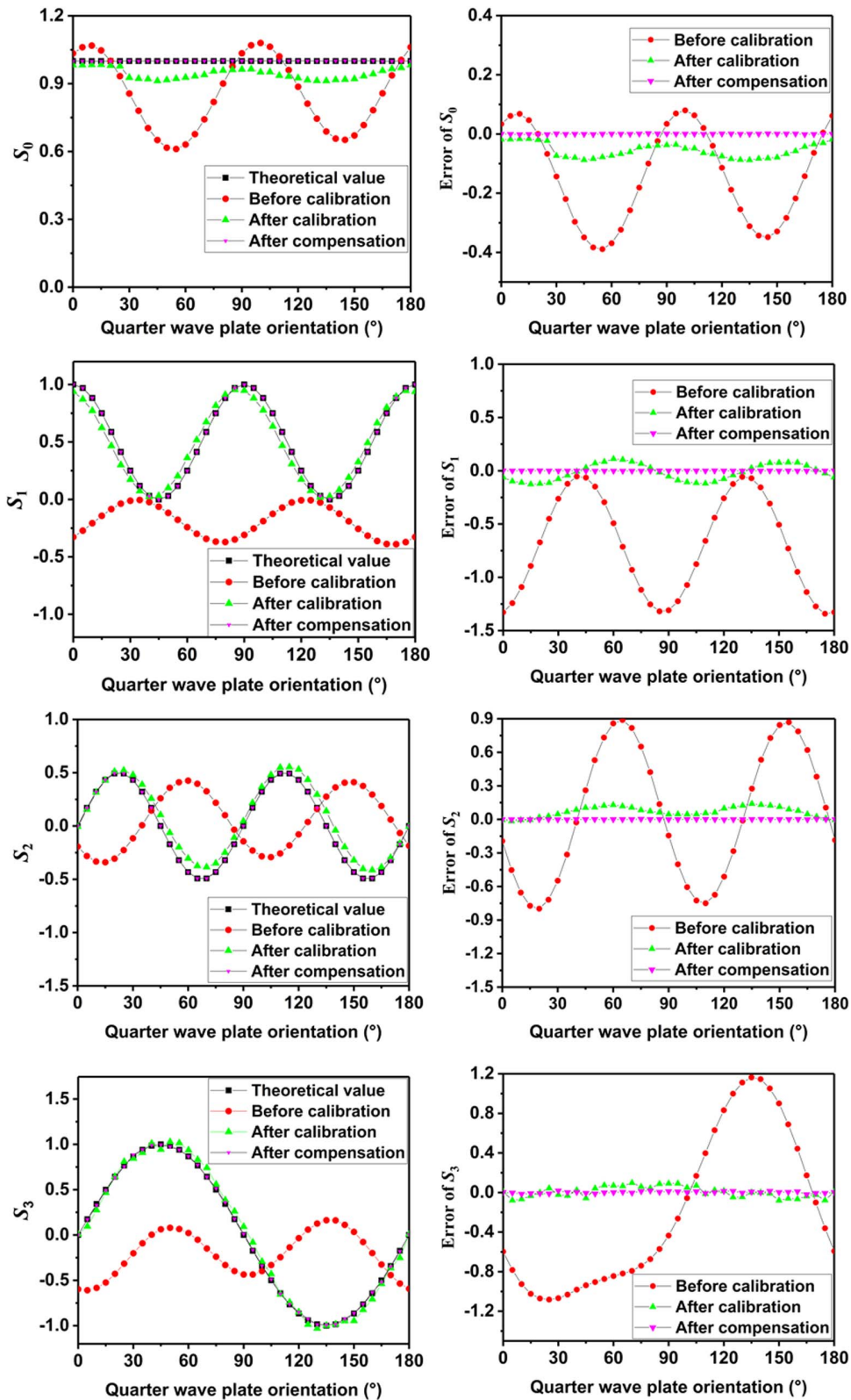

Fig. 8. Testing results of Stokes parameters. The subplots in the left column represent the theoretical and calculated pre-calibration, post-calibration, and post-compensation values of the Stokes parameters $S_0 - S_3$; the subplots in the right column represent the errors in the calculated pre-calibration, post-calibration, and post-compensation values of the Stokes parameters $S_0 - S_3$.
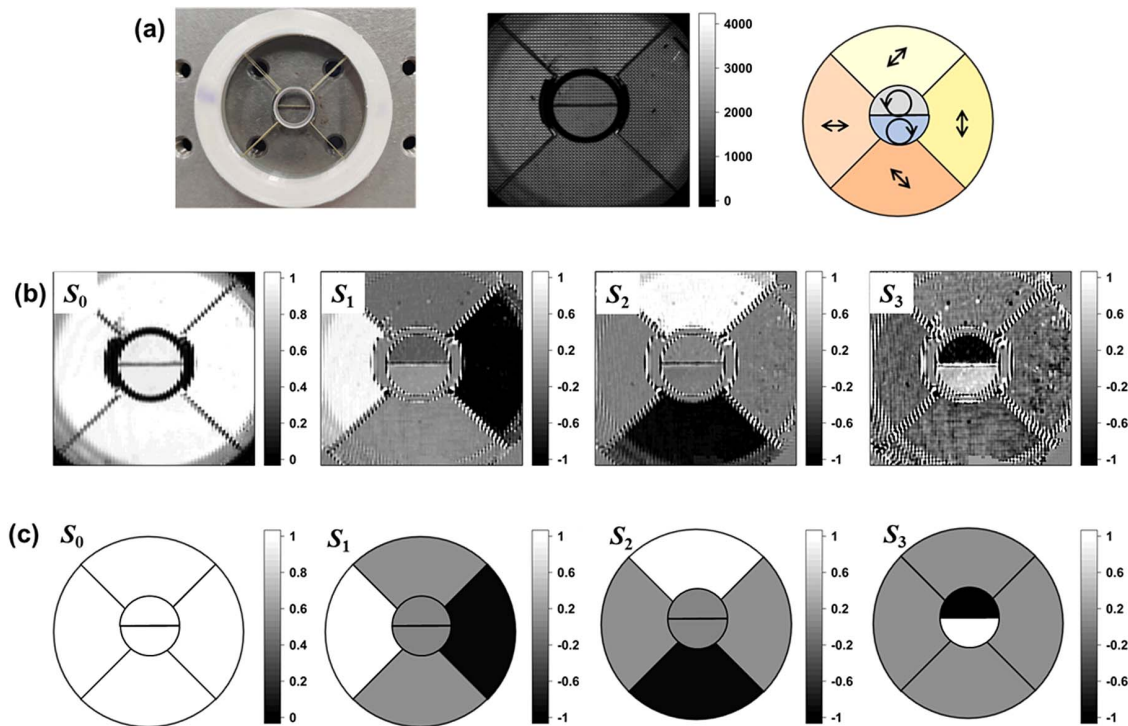
Fig. 9. Polarimetric imaging. (a) Physical image and its corresponding original imaging and polarization state schematic. (b) Calculated Stokes parameter image. (c) Theoretical Stokes parameter image of the targeted polarization mask.

errors, and the errors of the Stokes parameters inverted by the system matrix after calibration are 8.77%, 12.58%, 14.04%, and 25.96%, respectively. The inversion error of the Stokes parameters after calibration has a good regularity, which is related to the system error of the light source system. Therefore, this paper compensates for the system error. The compensation process involves conducting five experiments under the same experimental parameters and obtaining the average value of the inversion error, using the average value to compensate for the experimental results of the sixth group. The inversion errors of the compensated Stokes parameters are 0.21%, 0.21%, 0.42%, and 1.96%, respectively. In order to further verify the imaging effect of the full-Stokes polarization imaging system, this paper produces an imaging sample that includes linear polarization elements and circular polarization elements. Different orientations of linear polarization elements were achieved through 0°, 45°, 90°, and 135° linear polarizers, while different handednesses of circular polarization elements were achieved through 45° and 135° linear polarizers and a quarter-wave plate at 0° orientation. When the imaging sample was placed in front of the natural light source generated by the integrating sphere, polarized light with different polarization states was modulated and imaged by the polarized imaging system. Figure 9(a) shows the physical image of the sample, its corresponding original image, and a polarization state diagram. Through the physical image and original image, it can be found that the light intensity information of different polarization elements is basically the same, and it is difficult to identify them by eye or by intensity imaging. Figures 9(b) and 9(c) show the calculated Stokes parameter image and theoretical Stokes parameter image of the corresponding imaging sample. The

calculated results of the Stokes parameters have good consistency with the theoretical results. Among them, the S_0 image of the Stokes parameter represents the intensity image, which cannot distinguish between different polarization elements. Identification of different polarization elements can be achieved through the $S_1 – S_3$ images of the Stokes parameters. Compared with traditional intensity imaging systems, this imaging system can better apply to imaging and detection of polarization-sensitive targets.

4. CONCLUSION

In conclusion, a pixelated aluminium wire-grid-based metamaterial integrating the functions of both linear polarization filters and circular polarization filters was designed and fabricated. The aluminium wire-grid was designed as a linear polarization filter with an average linear polarization extinction ratio of 36,000 and circular polarization filter with an average circular polarization extinction ratio of 110 in the Vis-NIR. Large-area ultracompact 320×320 pixelated aluminium wire-grid-based full-Stokes metamaterials were fabricated by nanoimprint lithography and nano transfer printing with the advantages of low cost and high efficiency, and were used to realize full-Stokes polarization imaging with errors within 8.77%, 12.58%, 14.04%, and 25.96% for Stokes parameters S_0, S_1, S_2, and S_3, respectively. The inversion errors of the compensated Stokes parameters were reduced to 0.21%, 0.21%, 0.42%, and 1.96%, respectively. The design features an ultracompact layout and excellent polarization optics performance and capability of easy integration onto various types of Vis-NIR imaging detectors.

APPENDIX A: DEVICE FABRICATION

The fabrication process of large-area ultracompact pixelated aluminium wire-grid-based metamaterials is shown in Fig. 4. The intermediate polymer sheet (IPS), purchased from Obducat AB, is a kind of fluoropolymer material. The NIL and NTP were carried out on an Eitre 6-inch nanoimprinter (Obducat AB, Sweden).

Figure 4(a1). For the preparation of the IPS flexible template with 0°, 45°, 90°, and –45° orientation wire-grids, refer to [14].

Figure 4(a2). Formation of dielectric wire-grid on the quartz substrate precoated with a UV-curable photoresist by UV-curable NIL. First, spin-coating of 100 nm UV-curable nanoimprint photoresist on the surface of a cleaned quartz substrate and then baking at 95°C for 3 min. Finally, transfer of IPS flexible template structures to the quartz substrate by UV-curable nanoimprint lithography with 65°C imprinting temperature, 40 bar pressure, and 350 mJ cm^{-2} UV-exposure dose.

Figure 4(a3). Bilayer aluminium wire-grid-based LP filter micro arrays obtained by a vertical thermal evaporation process. The quartz substrate patterned with dielectric wire-grid micro arrays was placed horizontally with an aluminiun evaporation source. A chamber vacuum was pumped down to 10^{-4} Pa to avoid oxidation of aluminium in the evaporation process. In addition, 56 A evaporation current was selected to obtain smooth aluminium film, and the thickness of the aluminium film was 80 nm monitored by the quartz-crystal microbalance.

Figure 4(b1). Preparation of large-area IPS flexible template with single-directional wire-grid. The production process parameters were the same as Fig. 4(a1).

Figure 4(b2). Bilayer aluminium wire-grid structure obtained by a vertical thermal evaporation process. The thickness of the aluminium film was 12 nm monitored by the quartz-crystal microbalance, and other parameters are consistent with Fig. 4(a3).

Figure 4(c1). IPS surface metal nano wire-grid integrated onto the surface of the double-layer metal-aluminum nano wire-grid linear polarization filter micro array precoated with a UV-curable photoresist by a nano transfer printing process. First, spin-coating of 200 nm UV-curable nanoimprint photoresist on the surface of the linear polarization filter micro array and then baking at 95°C for 3 min. Then, the IPS surface metal nano wire-grid was integrated onto the surface of the double-layer metal-aluminum nano wire-grid linear polarization filter micro array by the NTP process [42]. The NTP temperature, pressure, and UV-exposure dose were 35°C, 10 bar, and 350 mJ cm^{-2}, respectively.

Figure 4(c2). Spin-coating of BP212 on linear polarization filter micro array. Spin-coating of a 2 μm BP212 photoresist on the surface of the sample and then baking at 85°C for 30 min.

Figure 4(c3). Formation of pixelated metamaterials integrating both linear polarization filters and circular polarization filters by photolithography, development, etching, and a residual adhesive removal process. First, the BP212 was exposed with exposure dose 300 mJ cm^{-2}. Then, the BP212 was developed for about 100 s by 0.5% hydroxide solution to remove the BP212 and aluminum in the exposure area. After that, the remaining BP212 was dissolved in acetone for 60 s, and then the sample was rinsed with deionized water for 60 s.

APPENDIX B: CALIBRATION OF THE IMAGING SYSTEM

Based on the structural characterization and optical performance measurement results, it is known that there are fabrication errors in micro array devices that affect the optical performance. In order to achieve full Stokes polarization imaging of the imaging system, the system needs to be calibrated. The relationship among the grayvalue of the camera response, the Stokes vector of incident light, and the system matrix of the device can be expressed by Eq. (B1):

$$I = \begin{bmatrix} I_0 \\ I_{45} \\ I_{90} \\ I_{CP} \end{bmatrix} = M \begin{bmatrix} S_0 \\ S_1 \\ S_2 \\ S_3 \end{bmatrix} = MS, \qquad \textbf{(B1)}$$

where I denotes the light intensity vector corresponding to the four polarization filters, M represents the system matrix of the device, and S denotes the Stokes vector of incident light. First, the Stokes vectors of multiple groups of incident light and their corresponding grayscale values of camera response are obtained; then the final system matrix of the device can be obtained using the least squares method. The calculation process can be expressed as Eqs. (B2) and (B3):

$$I' = \begin{bmatrix} I_0^{(1)} & I_0^{(2)} & I_0^{(3)} & \cdots & I_0^{(n)} \\ I_{45}^{(1)} & I_{45}^{(2)} & I_{45}^{(3)} & \cdots & I_{45}^{(n)} \\ I_{90}^{(1)} & I_{90}^{(2)} & I_{90}^{(3)} & \cdots & I_{90}^{(n)} \\ I_{CP}^{(1)} & I_{CP}^{(2)} & I_{CP}^{(3)} & \cdots & I_{CP}^{(n)} \end{bmatrix}$$

$$= M \begin{bmatrix} S_0^{(1)} & S_0^{(2)} & S_0^{(3)} & \cdots & S_0^{(n)} \\ S_1^{(1)} & S_1^{(2)} & S_1^{(3)} & \cdots & S_1^{(n)} \\ S_2^{(1)} & S_2^{(2)} & S_2^{(3)} & \cdots & S_2^{(n)} \\ S_3^{(1)} & S_3^{(2)} & S_3^{(3)} & \cdots & S_3^{(n)} \end{bmatrix}$$

$$= MS', \quad n = 1, 2, 3, \ldots, \qquad \textbf{(B2)}$$

$$M = I' \cdot S'^{-1}. \qquad \textbf{(B3)}$$

The system matrix has 16 unknown elements, so we need at least four sets of nonlinearly independent incident Stokes vectors and their corresponding intensity vectors to solve the system matrix. In this paper, we calibrate the system matrix by creating six standard polarized lights: 0°, 45°, 90°, and 135° linearly polarized light, as well as left and right circularly polarized light. This involves the following steps.

(1) Aligning the coordinate systems of the light source system and imaging system. A linear polarizer is placed on precision turntable 1 and a quarter-wave plate is fixed on precision turntable 2. First, by rotating the linear polarizer with precision turntable 1, the orientation of the outgoing polarized light is changed, while observing the grayscale value of the pixel corresponding to the zero-degree linear polarization unit. When the grayscale value response is maximum, the orientation of precision turntable 1 at this time is defined as 0°. Second, precision turntable 2 and the quarter-wave plate are placed in the optical path, and the orientation of the quarter-wave plate is

changed while observing the grayscale value of the pixel corresponding to the zero-degree linear polarizer element. When the grayscale value response is maximum, the orientation of precision turntable 2 at this time is defined as 0°.

(2) Creating six standard polarized lights. First, the angles of precision turntables 1 and 2 are simultaneously changed to generate 0°, 45°, 90°, and 135° linearly polarized light sequentially. Second, adjust the orientation of precision turntable 1 to 0°, and adjust the angle of precision turntable 2 to ±45° (counterclockwise rotation is positive; clockwise rotation is negative) to produce right and left circularly polarized light, respectively.

(3) Inverting the system matrix. Using the Stokes vector of the incident polarized light and its corresponding light intensity vector, the system matrix is inverted using the least squares method according to Eq. (B3).

Disclosures. The authors declare no conflicts of interest.

Data Availability. Data underlying the results presented in this paper are not publicly available at this time but may be obtained from the authors upon reasonable request.

REFERENCES

1. J. Wang, J. Yang, I. M. Fazal, N. Ahmed, Y. Yan, H. Huang, Y. Ren, Y. Yue, S. Dolinar, M. Tur, and A. E. Willner, "Terabit free-space data transmission employing orbital angular momentum multiplexing," Nat. Photonics **6**, 488–496 (2012).
2. A. Nicolas, L. Veissier, L. Giner, E. Giacobino, D. Maxein, and J. Laurat, "A quantum memory for orbital angular momentum photonic qubits," Nat. Photonics **8**, 234–238 (2014).
3. J. Li, S. Kamin, G. Zheng, F. Neubrech, S. Zhang, and N. Liu, "Addressable metasurfaces for dynamic holography and optical information encryption," Sci. Adv. **4**, r6768 (2018).
4. L. Jin, Z. Dong, S. Mei, Y. F. Yu, Z. Wei, Z. Pan, S. D. Rezaei, X. Li, A. I. Kuznetsov, Y. S. Kivshar, J. K. W. Yang, and C. Qiu, "Noninterleaved metasurface for $(2^6 - 1)$ spin- and wavelength-encoded holograms," Nano Lett. **18**, 8016–8024 (2018).
5. Y. Fan, R. Zhang, Z. Liu, and J. Chu, "A skylight orientation sensor based on S-waveplate and linear polarizer for autonomous navigation," IEEE Sens. J. **21**, 23551–23557 (2021).
6. Z. Wan, K. Zhao, and J. Chu, "Robust azimuth measurement method based on polarimetric imaging for bionic polarization navigation," IEEE Trans. Instrum. Meas. **69**, 5684–5692 (2020).
7. Y. Chen, J. Chu, F. Lin, B. Jiang, Y. Liu, B. Huang, R. Zhang, B. Xin, and X. Ding, "Polarization clustering of biological structures with Mueller matrix parameters," J. Biophoton. **16**, e202200255 (2022).
8. C. He, H. He, J. Chang, B. Chen, H. Ma, and M. J. Booth, "Polarisation optics for biomedical and clinical applications: a review," Light Sci. Appl. **10**, 194 (2021).
9. G. Zhang, X. Nie, and Z. Du, "Target polarization characteristics analysis and detection in complex background," J. Phys. Conf. Ser. **1914**, 12001 (2021).
10. P. Sun, D. Zeng, X. Li, L. Yang, L. Li, Z. Chen, and F. Chen, "A 3D mask presentation attack detection method based on polarization medium wave infrared imaging," Symmetry **12**, 376 (2020).
11. N. Short, S. Hu, P. Gurram, K. Gurton, and A. Chan, "Improving cross-modal face recognition using polarimetric imaging," Opt. Lett. **40**, 882–885 (2015).
12. V. Gruev, A. Ortu, N. Lazarus, J. Van der Spiegel, and N. Engheta, "Fabrication of a dual-tier thin film micropolarization array," Opt. Express **15**, 4994–5007 (2007).
13. X. Zhao, A. Bermak, F. Boussaid, T. Du, and V. G. Chigrinov, "High-resolution photoaligned liquid-crystal micropolarizer array for polarization imaging in visible spectrum," Opt. Lett. **34**, 3619–3621 (2009).
14. R. Zhang, Y. Fan, C. Wu, Z. Liu, and J. Chu, "Multidirectional mono-layer metal nano-grating micro polarizer array based on nanoimprint lithography and plasma ashing process," J. Micromech. Microeng. **29**, 125003 (2019).
15. B. Feng, Y. Chen, D. Sun, Z. Yang, B. Yang, X. Li, and T. Li, "Precision integration of grating-based polarizers onto focal plane arrays of near-infrared photovoltaic detectors for enhanced contrast polarimetric imaging," Int. J. Extreme Manuf. **3**, 35201 (2021).
16. X. Zhao, A. Bermak, F. Boussaid, and V. G. Chigrinov, "Liquid-crystal micropolarimeter array for full Stokes polarization imaging in visible spectrum," Opt. Express **18**, 17776–17787 (2010).
17. E. M. Sánchez-Carnerero, F. Moreno, B. L. Maroto, A. R. Agarrabeitia, M. J. Ortiz, B. G. Vo, G. Muller, and S. D. L. Moya, "Circularly polarized luminescence by visible-light absorption in a ChiralO-BODIPY dye: unprecedented design of CPL organic molecules from achiral chromophores," J. Am. Chem. Soc. **136**, 3346–3349 (2014).
18. E. Plum, V. A. Fedotov, and N. I. Zheludev, "Optical activity in extrinsically chiral metamaterial," Appl. Phys. Lett. **93**, 191911 (2008).
19. V. A. Fedotov, A. S. Schwanecke, N. I. Zheludev, V. V. Khardikov, and S. L. Prosvirnin, "Asymmetric transmission of light and enantiomerically sensitive plasmon resonance in planar chiral nanostructures," Nano Lett. **7**, 1996–1999 (2007).
20. A. S. Schwanecke, V. A. Fedotov, V. V. Khardikov, S. L. Prosvirnin, Y. Chen, and N. I. Zheludev, "Nanostructured metal film with asymmetric optical transmission," Nano Lett. **8**, 2940–2943 (2008).
21. K. A. Bachman, J. J. Peltzer, P. D. Flammer, T. E. Furtak, R. T. Collins, and R. E. Hollingsworth, "Spiral plasmonic nanoantennas as circular polarization transmission filters," Opt. Express **20**, 1308–1319 (2012).
22. J. K. Gansel, M. Thiel, M. S. Rill, M. Decker, K. Bade, V. Saile, G. von Freymann, S. Linden, and M. Wegener, "Gold helix photonic metamaterial as broadband circular polarizer," Science **325**, 1513–1515 (2009).
23. Z. Yang, M. Zhao, and P. Lu, "How to improve the signal-to-noise ratio for circular polarizers consisting of helical metamaterials?" Opt. Express **19**, 4255–4260 (2011).
24. R. Ji, S. Wang, X. Liu, H. Guo, and W. Lu, "Hybrid helix metamaterials for giant and ultrawide circular dichroism," ACS Photonics **3**, 2368–2374 (2016).
25. Z. Y. Yang, M. Zhao, P. X. Lu, and Y. F. Lu, "Ultrabroadband optical circular polarizers consisting of double-helical nanowire structures," Opt. Lett. **35**, 2588–2590 (2010).
26. Y. Yu, Z. Yang, S. Li, and M. Zhao, "Higher extinction ratio circular polarizers with hetero-structured double-helical metamaterials," Opt. Express **19**, 10886–10894 (2011).
27. J. K. Gansel, M. Latzel, A. Frölich, J. Kaschke, M. Thiel, and M. Wegener, "Tapered gold-helix metamaterials as improved circular polarizers," Appl. Phys. Lett. **100**, 101109 (2012).
28. J. Kaschke, M. Blome, S. Burger, and M. Wegener, "Tapered *N*-helical metamaterials with three-fold rotational symmetry as improved circular polarizers," Opt. Express **22**, 19936–19946 (2014).
29. Y. Cui, L. Kang, S. Lan, S. Rodrigues, and W. Cai, "Giant chiral optical response from a twisted-arc metamaterial," Nano Lett. **14**, 1021–1025 (2014).
30. M. Hentschel, V. E. Ferry, and A. P. Alivisatos, "Optical rotation reversal in the optical response of chiral plasmonic nanosystems: the role of plasmon hybridization," ACS Photonics **2**, 1253–1259 (2015).
31. Y. Zhao, M. A. Belkin, and A. Alù, "Twisted optical metamaterials for planarized ultrathin broadband circular polarizers," Nat. Commun. **3**, 870 (2012).
32. Y. He, G. K. Larsen, W. Ingram, and Y. Zhao, "Tunable three-dimensional helically stacked plasmonic layers on nanosphere monolayers," Nano Lett. **14**, 1976–1981 (2014).

33. G. K. Larsen, Y. He, W. Ingram, and Y. Zhao, "Hidden chirality in superficially racemic patchy silver films," Nano Lett. **13**, 6228–6232 (2013).

34. Y. He, G. Larsen, X. Li, W. Ingram, F. Chen, and Y. Zhao, "Nanoscale conical Swiss roll with broadband visible and NIR circular dichroism," Adv. Opt. Mater. **3**, 342–346 (2015).

35. J. Bai, C. Wang, X. Chen, A. Basiri, C. Wang, and Y. Yao, "Chip-integrated plasmonic flat optics for mid-infrared full-Stokes polarization detection," Photonics Res. **7**, 1051–1060 (2019).

36. A. Basiri, X. Chen, J. Bai, P. Amrollahi, J. Carpenter, Z. Holman, C. Wang, and Y. Yao, "Nature-inspired chiral metasurfaces for circular polarization detection and full-Stokes polarimetric measurements," Light Sci. Appl. **8**, 78 (2019).

37. I. Yamada, J. Nishii, and M. Saito, "Modeling, fabrication, and characterization of tungsten silicide wire-grid polarizer in infrared region," Appl. Opt. **47**, 4735–4738 (2008).

38. J. D. Baena, J. P. Del Risco, A. P. Slobozhanyuk, S. B. Glybovski, and P. A. Belov, "Self-complementary metasurfaces for linear-to-circular polarization conversion," Phys. Rev. B **92**, 245413 (2015).

39. Y. Fan, R. Zhang, Z. Liu, C. Guan, and J. Chu, "Broadband linear-to-circular polarization converter based on ultrathin metal nano-grating," in *16th IEEE International Conference on Nano/Micro Engineered and Molecular Systems (IEEE-NEMS)* (2021), pp. 372–375.

40. Y. Fan, J. Chu, R. Zhang, Z. Liu, C. Guan, J. Liu, and Z. Zhang, "Broadband Vis-NIR circular polarizer with cascaded aluminium wire-grid," Adv. Mater. Technol. **8**, 2201394 (2022).

41. C. Wu, R. Zhang, Y. Fan, and J. Chu, "Convolution interpolation for division of focal plane polarimeter," Acta Photonica Sin. **48**, 178–186 (2019).

42. Y. Fan, R. Zhang, Z. Liu, D. Huang, and J. Chu, "Direct metallic nano-structures transfer by flexible contact UV-curable nano-imprint lithography," Appl. Phys. Express **12**, 095004 (2019).